Dendritic trafficking faces physiologically critical speed-precision tradeoffs

Alex H. Williams[1,2,3,*], **Cian O'Donnell**[2,4], **Terrence Sejnowski**[2,5], **and Timothy O'Leary**[6,7,*]

[1]Department of Neurosciences, University of California, San Diego, La Jolla, CA 92093, USA
[2]Howard Hughes Medical Institute, Salk Institute for Biological Studies, La Jolla, CA 92037, USA
[3]Department of Neurobiology, Stanford University, Stanford, CA 94305, USA
[4]Department of Computer Science, University of Bristol, Woodland Road, Bristol, BS8 1UB, United Kingdom
[5]Division of Biological Sciences, University of California at San Diego, La Jolla, CA 92093, USA
[6]Volen Center and Biology Department, Brandeis University, Waltham, MA 02454, USA
[7]Department of Engineering, University of Cambridge, Trumpington St, Cambridge, CB2 1PZ, United Kingdom
[*]Address correspondence to: ahwillia@stanford.edu, timothy.oleary@eng.cam.ac.uk

ABSTRACT

Nervous system function requires intracellular transport of channels, receptors, mRNAs, and other cargo throughout complex neuronal morphologies. Local signals such as synaptic input can regulate cargo trafficking, motivating the leading conceptual model of neuron-wide transport, sometimes called the "sushi-belt model" (Doyle and Kiebler, 2011). Current theories and experiments are based on this model, yet its predictions are not rigorously understood. We formalized the sushi belt model mathematically, showing how it can achieve arbitrarily complex spatial distributions of cargo in reconstructed morphologies. However, the model also predicts an unavoidable, morphology dependent tradeoff between speed, precision and metabolic efficiency of cargo transport. With experimental estimates of trafficking kinetics, the model predicts delays of many hours or days for modestly accurate and efficient cargo delivery throughout a dendritic tree. These findings challenge current understanding of the efficacy of nucleus-to-synapse trafficking and may explain the prevalence of local biosynthesis in neurons.

Keywords: Regulation, Active transport, Plasticity, Tagging hypothesis, Morphology, Motor proteins

INTRODUCTION

Dendritic and axonal trees of neurons often have many tens or even thousands of branches that can extend across the entire nervous system. Distributing biomolecular cargo within neuronal morphologies is therefore a considerable logistical task, especially for components that are synthesized in locations distant from their site of use. Nonetheless, molecular transport is important for many neurophysiological processes, such as synaptic plasticity, neurite development and local metabolism. For example, long-lasting forms of synaptic plasticity appear to depend on anterograde transport of mRNAs (Nguyen et al., 1994; Bading, 2000; Kandel, 2001) and specific mRNAs are known to be selectively transported to regions of heightened synaptic activity (Steward et al., 1998; Steward and Worley, 2001; Moga et al., 2004) and to developing synaptic contacts (Lyles et al., 2006).

On the other hand, local biosynthesis and component recycling are known to support dendritic physiology, including some forms of synaptic plasticity (Kang and Schuman, 1996; Aakalu et al., 2001; Vickers et al., 2005;

Sutton and Schuman, 2006; Holt and Schuman, 2013) and maintenance of cytoskeletal, membrane and signaling pathways (Park et al., 2004, 2006; Grant and Donaldson, 2009; Zheng et al., 2015). Neurons therefore rely on a mixture of local metabolism and global transport, but the relative contributions of these mechanisms are not understood. Analyzing the performance of global trafficking provides a principled way to understand the division of labor between local and global mechanisms.

In this paper we ask a simple question: how well can trafficking perform globally, given what we know about active transport and the typical morphologies of neurites? There are two parts to this question. First, how can active transport achieve specific spatial distributions of cargo using only local signals? Second, how long does it take to distribute cargo to a given degree of accuracy and what factors contribute to delays?

Intracellular trafficking mechanisms are being characterized in increasing detail (Buxbaum et al., 2014b; Hancock, 2014; Wu et al., 2016). Microscopic cargo movements are stochastic, bidirectional, and inhomogeneous along neurites, leading to to the hypothesis that trafficking is predominantly controlled by local pathways that signal demand for nearby cargo, rather than a centralized addressing system (Welte, 2004; Bressloff and Newby, 2009; Newby and Bressloff, 2010a; Doyle and Kiebler, 2011; Buxbaum et al., 2015). These local signals are not fully characterized, but there is evidence of multiple underlying mechanisms including transient elevations in second-messengers like $[Ca^{2+}]$ and ADP (Mironov, 2007; Wang and Schwarz, 2009), glutamate receptor activation (Kao et al., 2010; Buxbaum et al., 2014b), and changes in microtubule-associated proteins (Soundararajan and Bullock, 2014).

A leading conceptual model ties together these details by proposing that bidirectional trafficking, combined with local signalling determines the spatial distribution of cargo in neurons (Welte, 2004; Buxbaum et al., 2015). Doyle and Kiebler (2011) call this the "sushi belt model". In this analogy, molecular cargoes are represented by sushi plates that move along a conveyor belt, as in certain restaurants. Customers sitting alongside the belt correspond to locations along a dendrite that have specific and potentially time-critical demand for the amount and type of sushi they consume, but they can only choose from nearby plates as they pass.

Stated in words, the sushi belt model is an intuitive, plausible account of the molecular basis of cargo distribution. Yet it is unclear whether this model conforms to intuition, and whether it implies hidden, biological relevant and testable predictions. Can this trafficking system accurately generate global distributions of cargo using only local signals? Does the model predict cross-talk, or interference between spatially separated regions of the neuron that require the same kind of cargo? How quickly and how accurately can cargo be delivered by this model, given what is know about trafficking kinetics, and do these measures of performance depend on morphology or the spatial pattern of demand?

We address these questions using simple mathematical models that capture experimentally measured features of trafficking. We confirm that the sushi-belt model can produce any spatial distribution of cargo in complex morphologies. However, the model also predicts that global trafficking from the soma is severely limited by tradeoffs between the speed, efficiency, robustness, and accuracy of cargo delivery. Versions of the model predict testable interactions between trafficking dependent processes, while the model as a whole suggests that time-critical processes like synaptic plasticity may be less precise, or less dependent on global transport than is currently assumed.

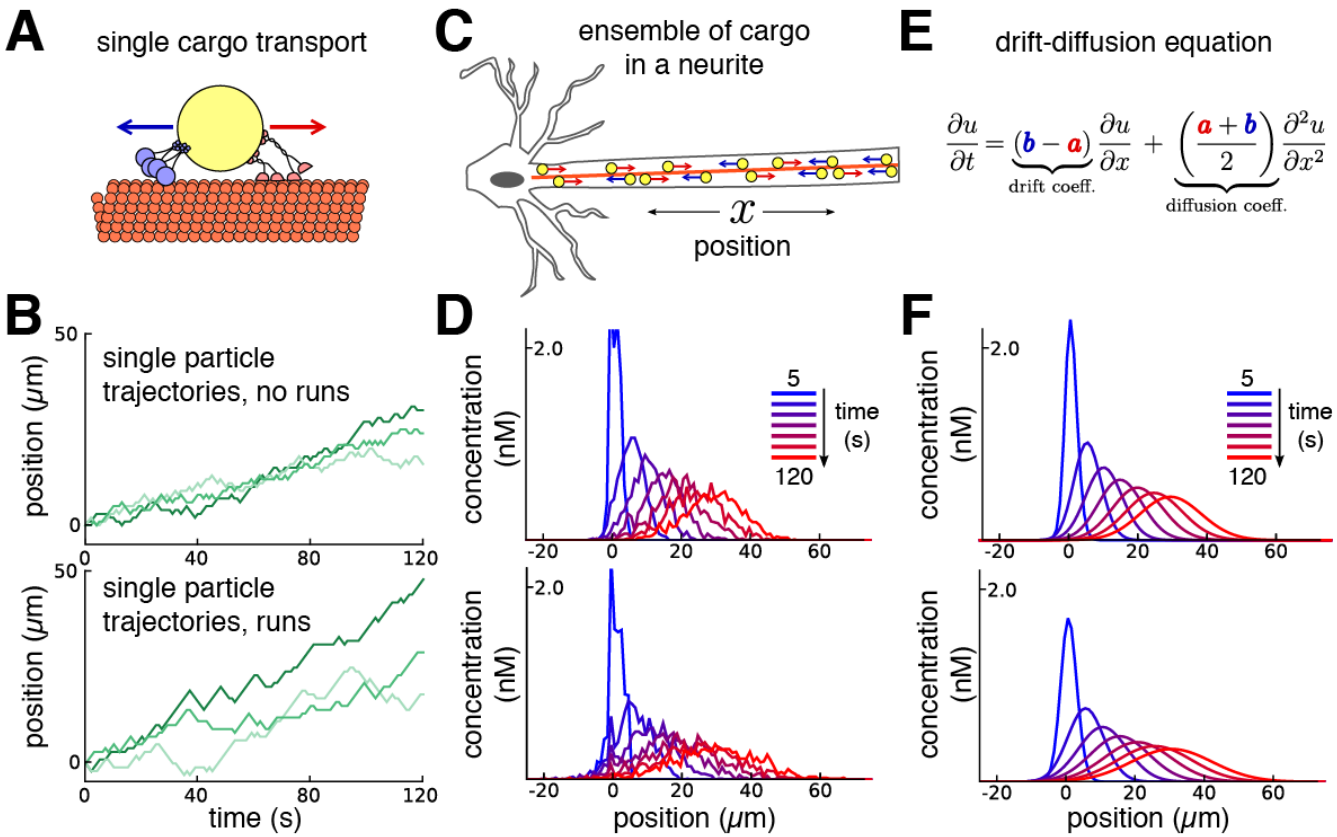

Figure 1. Constructing a coarse-grained model of intracellular transport. **(A)** Cartoon of a single cargo particle on a microtubule being subjected to stochastic back-and-forth movements driven by opposing motor proteins. **(B)** Three example biased random walks, representing the movement of individual cargoes. (Top panel) A simple random walk with each step independent of previous steps. (Bottom panel) adding history-dependence to the biased random walk results in sustained unidirectional runs and stalls in movement. **(C)** Cartoon of a population of cargo particles being transported along the length of a neurite. **(D)** Concentration profile of a population cargo transported along a neurite over time, simulated as 1,000 independent random walks. (Top panel) simulations without runs. (Bottom panel) simulations with runs. **(E)** In the limit of many individual cargo particles, the concentration of particles u is described by a drift diffusion model whose parameters, a and b, map onto the mass action model, (equation 1). **(F)** The mass-action model provides a good fit to the simulations of bulk cargo movement in (D). (Top panel) fitted trafficking rates for the model with no runs were $a \approx 0.42$ s^{-1}, $b \approx 0.17$ s^{-1}. (Bottom panel) fitting the model with runs gives $a \approx 0.79$ s^{-1}, $b \approx 0.54$ s^{-1}.

RESULTS

A simple model captures bulk behaviour of actively transported cargo

Transport along microtubules is mediated by kinesin and dynein motors that mediate anterograde and retrograde transport respectively (Block et al., 1990; Hirokawa et al., 2010; Gagnon and Mowry, 2011). Cargo is often simultaneously bound to both forms of motor protein, resulting in stochastic back-and-forth movements with a net direction determined by the balance of opposing movements (Welte, 2004; Hancock, 2014; Buxbaum et al., 2014a, Fig. 1A). We modeled this process as a biased random walk, which is general enough to accommodate variations in biophysical details (Bressloff, 2006; Bressloff and Earnshaw, 2007; Müller et al., 2008; Bressloff and Newby, 2009;

Newby and Bressloff, 2010a; Bressloff and Newby, 2013).

Figure 1 shows this model in a one-dimensional cable, corresponding to a section of neurite. In each unit of time the cargo moves a unit distance forwards or backwards, or remains in the same place, each with different probabilities. In the simplest version of the model, the probabilities of forward and backward jumps are constant for each time step (Fig. 1B, top panel). Cargo can also undergo extended unidirectional runs (Klumpp and Lipowsky, 2005; Müller et al., 2008; Hancock, 2014). The model can account for these runs with jump probabilities that depend on the previous movement of the particle (Fig. 1B, bottom panel, *Methods*).

While the movement of individual cargoes is stochastic, the movement of a population of cargoes (Fig. 1C) is predictable. This is seen in Figure 1D, which shows the distribution of 1000 molecules over time, with (top panel) and without (bottom panel) unidirectional runs. The bulk distribution of cargo can therefore be modeled as a deterministic process that describes how cargo cargo concentration spreads out in time. This leads to the well known drift-diffusion equation (Fig. 1E) when the movement probabilities are spatially uniform.

For simulations and calculations, this process can also be conveniently described by a mass-action model (Voit et al., 2015) that breaks up the concentration profile along a neurite into small compartments with concentration-dependent transition rates between adjacent comparments. In a neurite with N compartments, the mass-action model is:

$$u_1 \underset{b_1}{\overset{a_1}{\rightleftharpoons}} u_2 \underset{b_2}{\overset{a_2}{\rightleftharpoons}} u_3 \underset{b_3}{\overset{a_3}{\rightleftharpoons}} \ \ldots \ \underset{b_{N-1}}{\overset{a_{N-1}}{\rightleftharpoons}} u_N \tag{1}$$

where u_i is the amount of cargo in each compartment, and a_i and b_i respectively denote local rate constants for anterograde and retrograde transport. The parameters of the mass-action model map onto the drift-diffusion equation when rate constants are spatially homogeneous (Smith and Simmons, 2001). This allowed us to constrain mass-action model parameters using experimental estimates of the mean and variance of particle positions from imaging experiments (see *Methods*).

For example, with a compartment length of 1 μm, the simulations in figure 1D gave mean particle velocities of 15 μm per minute, which is within the range of experimental observations for microtubule transport (Rogers and Gelfand, 1998; Dynes and Steward, 2007; Müller et al., 2008). The variances of the particle distributions depended on whether unidirectional runs are assumed, and respectively grew at a rate of $\sim$0.58 and $\sim$1.33 μm^2 per second for the top and bottom panel of 1D. The mass action model provides a good fit to cases (Figure 1F). In general, the apparent diffusion coefficient of the model increases as run length increases (Figure 1 Supplement, 1A). The fit of the mass-action model decreases as the run length increases. However, the model remains a reasonable approximation for many physiological run lengths and particle numbers, even over a relatively short time window of 100 seconds (Figure 1 Supplement, 1B).

Biophysical formulation of the sushi belt model

The advantage of the mass action model is that it easily extends to complex morphologies with spatially non-uniform trafficking rates, and can accommodate additional processes, including sequestration of cargo. The sushi-belt model (Doyle and Kiebler, 2011) proposes that local mechanisms modify local trafficking rates and capture cargo as it passes. For these local signals to encode the demand for cargo, some feedback mechanism must exist between the local concentration of cargo and the signal itself. There are many biologically plausible mechanisms for locally encoding demand (see *Methods*). For our main results, we did not focus on these implementation details and simply assumed a reliable local demand signal. We have thus addressed the performance of the transport mechanism per se,

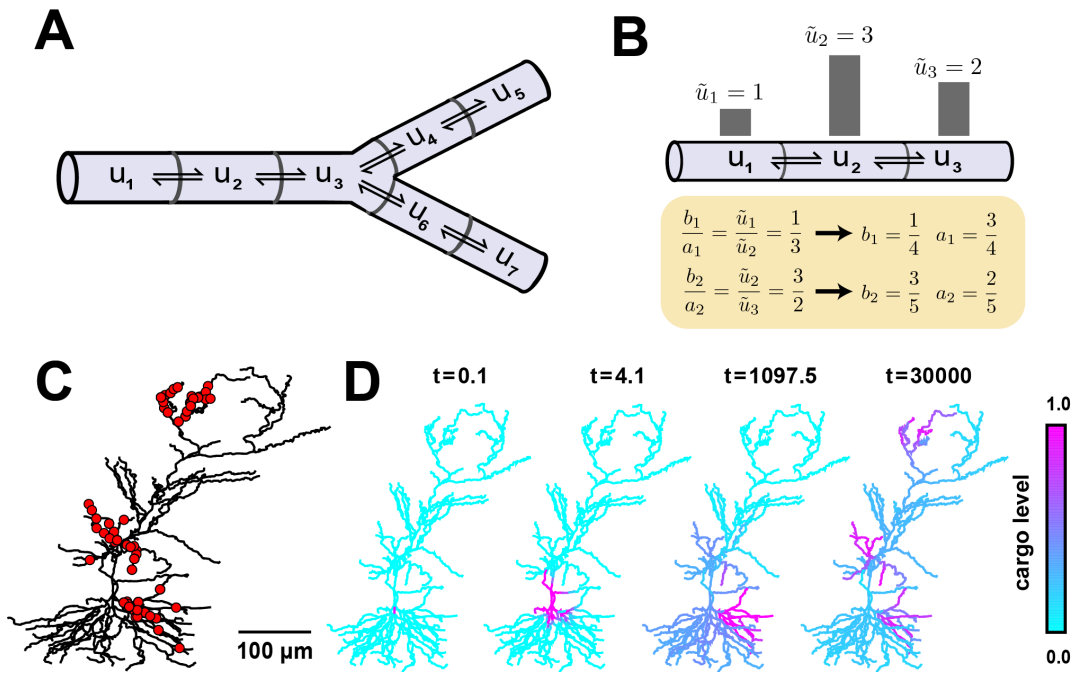

Figure 2. Local trafficking rates determine the spatial distribution of biomolecules by a simple kinetic relationship. **(A)** The mass action transport model for a simple branched morphology. **(B)** Demonstration of tuning trafficking rates to distribute cargo to match a demand signal. Each pair of rate constants ($\{a_1, b_1\}$, $\{a_2, b_2\}$) was constrained to sum to one. This constraint, combined with the condition in equation (4) specifies a unique solution to achieve the demand profile. **(C)** A model of a CA1 pyramidal cell with 742 compartments adapted from Migliore and Migliore (2012). Spatial cargo demand was set proportional to the average membrane potential deflection due to excitatory synaptic input applied at the locations marked by red dots. **(D)** Convergence of the cargo concentration in the CA1 model over time, t (arbitrary units).

under the most forgiving assumptions about how reliably demand is encoded.

The mass action model of sushi-belt transport is:

$$\begin{array}{ccccccccc} u_1 & \underset{b_1}{\overset{a_1}{\rightleftharpoons}} & u_2 & \underset{b_2}{\overset{a_2}{\rightleftharpoons}} & u_3 & \underset{b_3}{\overset{a_3}{\rightleftharpoons}} & u_4 & \underset{b_4}{\overset{a_4}{\rightleftharpoons}} & \dots \\ \downarrow{\scriptstyle c_1} & & \downarrow{\scriptstyle c_2} & & \downarrow{\scriptstyle c_3} & & \downarrow{\scriptstyle c_4} & & \\ u_1^\star & & u_2^\star & & u_3^\star & & u_4^\star & & \end{array} \tag{2}$$

where u represents the concentration of cargo on the network of microtubules, indexed by the compartment. In each compartment, molecules can irreversibly detach from the microtubules in a reaction $u_i \xrightarrow{c_i} u_i^\star$, where $u^\star$ denotes the detached cargo. Biologically, cargo will eventually degrade. However, in this study we are concerned with how cargo can be rapidly distributed so that detached cargo can satisfy demand for at least some time. Therefore, for simplicity we assume degradation rates are effectively zero.

In the limiting case where detachment rates also approach zero, we only need to consider trafficking between compartments, as shown in Figure 2A. Over time, concentrations of microtubule-bound cargo in each compartment approach steady-state, which occurs when the ratio of cargo between neighboring compartments is balanced by the

trafficking rates:

$$\left.\frac{u_p}{u_c}\right|_{ss} = \frac{b}{a} \tag{3}$$

where u_p is the level in a "parent" compartment (closer to soma), u_c is the level in the adjacent "child" compartment (closer to periphery) and b and a are the trafficking rate constants between these compartments.

If $\tilde{u}_i$ represents the local demand signal in compartment i, then equation (3) gives the condition for cargo distribution to match demand:

$$\frac{b}{a} = \frac{\tilde{u}_p}{\tilde{u}_c} \tag{4}$$

An example demand profile and the corresponding trafficking rate relationships are shown in Figure 2B. This condition ensures that cargo is delivered in proportion to local demand. The absolute concentration at steady-state is determined by the total amount of cargo produced (Figure 2, supplement 1); in the case of mRNA, this might be controlled at the somatic compartment by transcriptional regulation. In this paper, we mainly focus on the relative accuracy of cargo distribution when some fixed amount of cargo is produced at the soma.

To illustrate demand-modulated trafficking in a realistic setting, we used a reconstructed model of a CA1 pyramidal neuron (Migliore and Migliore, 2012). To provide a demand signal, we modeled excitatory synaptic input at 120 locations within three dendritic regions (red dots, Fig. 2D) and set demand, ($\tilde{u}_i$), equal to the average membrane potential in each electrical compartment (see *Methods*). As expected, cargo was transported selectively to regions of high synaptic activity (Fig. 2E, Supp. Movie 1), matching the demand profile exactly at steady state (Fig. 2F). Therefore, local control of trafficking rates (equivalently, motor protein kinetics) can deliver cargo to match arbitrarily complex spatial demand.

Transport bottlenecks occur when trafficking rates are non-uniform

If cargo delivery is achieved by controlling trafficking along microtubules, then delivery times to distal sites will be affected by proximal demand. For example, if the demand signal $\tilde{u}_i$ approaches zero in a compartment, the trafficking rates into that compartment also approach zero, cutting off the flow of cargo along the neurite (Fig 3A). The smallest demand signal, ε often determines the rate-limiting time constant for cargo delivery to an entire dendritic tree. We refer to this scenario as a "transport bottleneck." Figures 3B-C illustrate how decreasing ε to zero causes arbitrarily slow convergence in a simple 3-compartment model with all other trafficking rates normalized to 1.

We imposed a bottleneck in the reconstructed CA1 model by setting demand in the middle third of the apical dendrite to a lower level than the rest of the dendritic tree, which was set uniformly high. As expected, the cargo distribution converged much more quickly for uniform demand than with a bottleneck present (Fig. 3D).

However, less intuitive effects are seen on the convergence times of cargo in specific compartments. Figure 3E plots convergence time for u_i to reach a fraction of the steady state value for all compartments. While distal compartments showed prolonged convergence times, (Fig. 3E, upper right portion of plot), the bottleneck *shortened* the transport delay to proximal compartments (Fig. 3E, lower left portion of plot). This occurs because the bottleneck decreases the effective size of proximal part the neuron: cargo spreads efficiently throughout the proximal dendrites, but traverses the bottleneck more slowly.

Another counterintuitive effect is seen when demand varies independently at proximal and distal locations, as might occur during selective synaptic stimulation (see e.g., Han and Heinemann, 2013). In Figure 3F we simulated demand at proximal and distal portions of the apical dendrite independently and quantified the total convergence

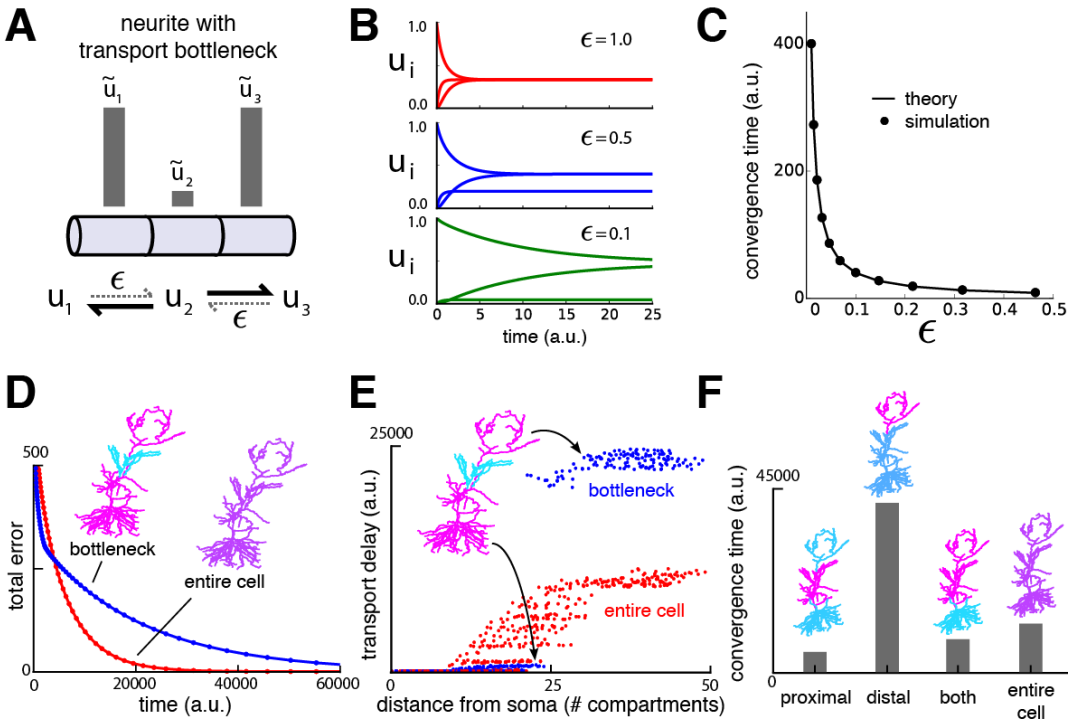

Figure 3. Transport bottlenecks caused by local demand profile. **(A)** A three-compartment transport model, with the middle compartment generating a bottleneck. The vertical bars represent the desired steady-state concentration of cargo in each compartment. The rate of transport into the middle compartment is small (ϵ, dashed arrows) relative to transport out of the middle compartment. **(B)** Convergence of cargo concentration in all compartments of model in (A) for decreasing relative bottleneck flow rate, ϵ. **(C)** Simulations (black dots) confirm that the time to convergence is given by the smallest non-zero eigenvalue of the system (solid curve). **(D)** Convergence to a uniform demand distribution (red line) is faster than a target distribution containing a bottleneck (blue line) in the CA1 model. Total error is the sum of the absolute difference in concentration from demand (L_1 norm). Neuron morphologies are color-coded according to steady state cargo concentration. **(E)** Transport delay for each compartment in the CA1 model (time to accumulate 0.001 units of cargo). **(F)** Bar plot comparison of convergence times for different spatial demand distributions in the CA1 model (steady-state indicated in color plots). The timescale for all simulations in the CA1 model was normalized by setting $a_i + b_i = 1$ for each compartment.

time. Proximal demand alone (Fig. 3F 'proximal') resulted in the fastest convergence time. Convergence was slowest when the demand was restricted to distal dendrites (Fig. 3F, 'distal'). Interestingly, when both distal and proximal sites signalled demand (Fig. 3F 'both'), convergence was substantially faster, even though cargo still needed to reach the distal neurites. Uniform demand across the entire tree (Fig. 3F 'entire cell') resulted in a similar shortening of convergence time.

Together, these results show that locally modulating trafficking movements will have testable effects on global transport times. The presence and relative contribution of this mechanism can be probed experimentally by characterizing the convergence rate of a cargo that aggregates at recently activated synapses, such as *Arc* mRNA (Steward et al., 1998).

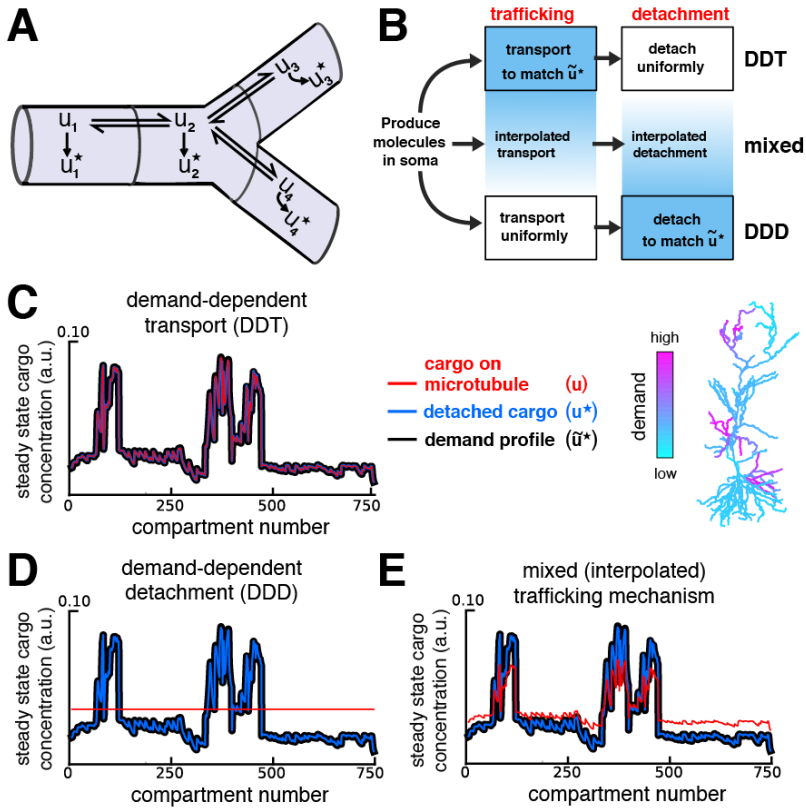

Figure 4. Multiple strategies for transport with trafficking and cargo detachment controlled by local signals. **(A)** Schematic of microtubular transport model with irreversible detachment in a branched morphology. **(B)** Multiple strategies for trafficking cargo to match local demand (demand = $\tilde{u}^\star$). (Top) The demand-dependent trafficking mechanism (DDT). When the timescale of detachment is sufficiently slow, the distribution of cargo on the microtubules approaches a quasi-steady-state that matches $\tilde{u}^\star$ spatially. This distribution is then transformed into the distribution of detached cargo, $u^\star$. (Bottom) The demand dependent detachment (DDD) mechanism. Uniform trafficking spreads cargo throughout the dendrites, then demand is matched by slowly detaching cargo according to the local demand signal. An entire family of mixed strategies is achieved by interpolating between DDT and DDD. **(C-E)** Quasi-Steady-state distribution of cargo on the microtubules (u, red) and steady-state distribution of detached cargo ($u^\star$, blue), shown with a demand profile ($\tilde{u}^\star$, black) for the various strategies diagrammed in panel B. The demand profile is shown spatially in the color-coded CA1 neuron in the right of panel C. Detached cargo matches demand in all cases.

Local control of trafficking and detachment results in a family of trafficking strategies

We next considered how detachment rates can be controlled by local demand signals. If trafficking is much faster than detachment ($a, b \gg c$), then the previous analysis remains valid because the distribution of u approaches a quasi-steady state that matches demand along the microtubules; cargo may then detach at a slow, nonspecific rate ($c_i =$ constant, with $c \ll a, b$). Figure 4C shows an example of this scenario, which we call *demand-dependent trafficking* (DDT). The spatial distribution of cargo is first achieved along the microtubules (red line, Fig. 4C), and maintained as cargo detaches (blue line, Fig. 4C).

In another limiting case, trafficking rates are spatially uniform ($a_i = b_i$) so that cargo spreads evenly along the

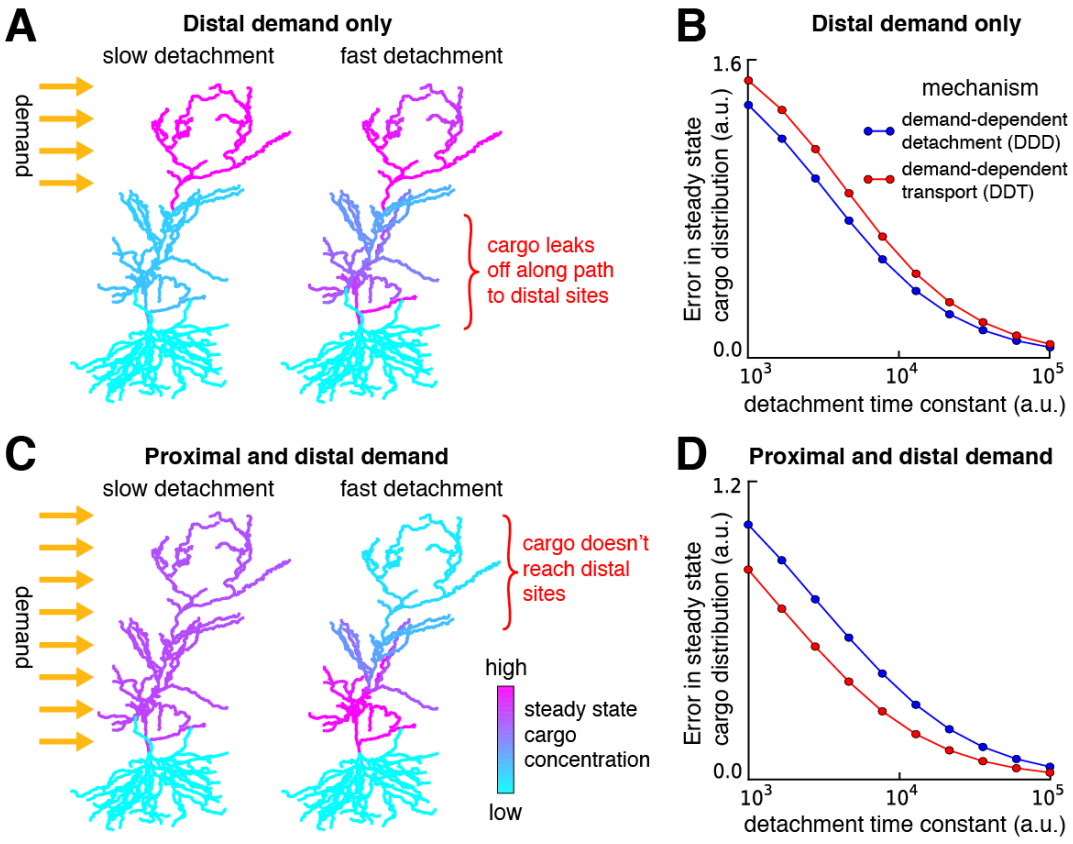

Figure 5. Tradeoffs in the performance of trafficking strategies depends on the spatial pattern of demand. **(A)** Delivery of cargo to the distal dendrites with slow *(left)* and fast detachment rates *(right)* in a reconstructed CA1 neuron. The achieved pattern does not match the target distribution when detachment is fast, since some cargo is erroneously delivered to proximal sites. **(B)** Tradeoff curves between spatial delivery error and convergence rate for the DDD and DDT trafficking strategies (blue line, see Fig 4D; red line, see Fig 4C). **(C-D)** Same as **(A-B)** but with a demand throughout proximal and distal locations. The timescale of all simulations was set by imposing the constraint that $a_i + b_i = 1$ for each compartment to permit comparison.

microtubules. The demand profile is then satisfied if local detachment rates are proportional to the demand level, $\tilde{u}^\star$:

$$c_i \propto \frac{\tilde{u}_i^\star}{\tilde{u}_i} \tag{5}$$

The result of this strategy, which we call *demand-dependent detachment* (DDD), is shown in Figure 4D. Unlike DDT, DDD avoids the transport bottlenecks examined in Figure 3, and can achieve target patterns with $\tilde{u}^\star$ equal to zero in certain compartments by setting $c_i = 0$.

The model can capture mixed transport strategies between these two extremes by interpolating the relationships between local demand, trafficking and transport rates (see *Methods*). Figure 4E shows the behavior of an intermediate model, whose parameters are a linear interpolation between pure DDT and DDD.

Rapid cargo delivery in the sushi-belt model is error-prone

Although it is mathematically convenient to separate the timescales of trafficking and detachment in the model, this separation may not exist in biological systems tuned for rapid transport. However, removal of timescale separation in the sushi-belt model results in mistargeted delivery of cargo, as we now show.

We returned to the CA1 model of Figure 4 and considered a scenario where there is demand for cargo at the distal apical dendrites (Fig. 5A). If the detachment rate constants are sufficiently slow, then, as before, delivered cargo matched demand nearly exactly in both the DDT and DDD models (Fig. 5A, left). However, increasing detachment rates led to faster convergence, but resulted in cargo leaking off the microtubule on the way to its destination (Fig. 5A, right). Thus, for a fixed trafficking timescale there is a tradeoff between the speed and accuracy of cargo delivery. The tradeoff curve shown in figure 5B (top) shows that both accuracy and convergence time decreased smoothly as the detachment rates were increased. This tradeoff was present regardless of whether the trafficking rates (Fig. 5B, red line) or detachment rates (Fig. 5B, blue line) were modified to meet demand (compare to Fig. 4C and 4D, respectively). However, DDD outperformed DDT overall, because the latter caused bottlenecks in proximal dendrites.

When the entire apical tree was stimulated, fast detachment prevented cargo delivery to distal synaptic sites (Fig. 5C, right). As before, a smooth speed-accuracy tradeoff is present for both transport strategies (Fig. 5D), but in contrast to distal demand alone, the DDT model outperformed DDD in this scenario (in contrast to Fig. 5A-B). Intuitively, DDT is better in this case because DDD results in cargo being needlessly trafficked to the basal dendrites.

Together, these results show that increasing the speed of cargo delivery comes at the cost of accuracy, and that the performance of different trafficking strategies depends on the spatial profile of demand. A family of models captures many possible variants of the sushi belt model with different relationships between the rates of underlying trafficking and detachment processes. This allowed us to assess how well trafficking can be expected to perform globally, without confining the results to specific cases.

We systematically estimated the severity of the speed-accuracy trade-off for biologically realistic neurite lengths and trafficking kinetics, with various spatial distributions of demand. Best-case estimates of drift-diffusion parameters predicted a severe tradeoff: a delay of 1 day to deliver cargo with 10% average error, and roughly a week to deliver within 1% average error (Figure 5 supplement 1, Supplemental movies 2-3).

Fine-tuned trafficking rates and cargo recycling introduce new tradeoffs

We asked whether the speed-precision tradeoff could be overcome by fine-tuning trafficking parameters or allowing cargo to be recycled instead of irreversibly detached.

First, we considered the effect of tuning anterograde trafficking rates to boost delivery to distal dendrites. We examined a realistic neurite length (800 μm; Figure 5 supplement 1, supplemental movie 4). Tuning the trafficking rates using a linear spatial gradient provided accurate and fast delivery (within 10% error in 200 minutes) when cargo demand was even along the cable. However, trafficking was very sensitive to changes in the spatial pattern of demand. Randomly altering the spatial profile of demand resulted in speed/precision performance that was comparable or worse than the untuned trafficking mechanisms, whose performance less sensitive to demand patterns (Figure 5, supplement 1, panels D-E).

Second, we considered a variant of the sushi-belt model that allowed for the reversible detachment/reattachment

of cargo from the microtubules (Figure 5, supplement 2):

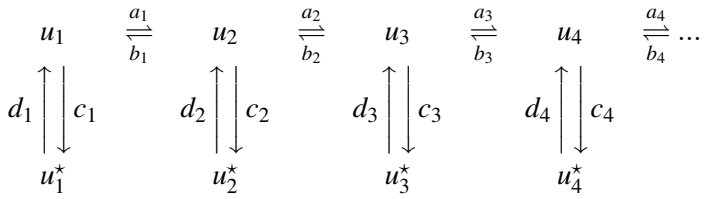

(6)

Inspection of this scheme reveals that it is similar in form to the DDT model analyzed in figures 2 & 3: the reversible detachment step simply adds and additional transient state in each compartment. As we noted in the DDT model, cargo distributions can match demand over time with arbitrarily low error (see equation 4). However, transport delays still exist. While releasing cargo to the wrong location is not an irreversible error, it slows delivery by temporarily arresting movement — known as a "diffusive trap" (see e.g. Bressloff and Earnshaw, 2007).

Cargo recycling creates a new tradeoff between delivery speed and excess cargo that has not found a destination. Models that deliver a high percentage of their cargo ($c_i > d_i$) converged on a similarly slow timescale to the cannonical sushi-belt model, since they greedily release cargo into the diffusive traps. Constraining excess cargo to 10% requires more than $\sim 10^3$ minutes for the demand profile to be matched within 10% (Figure 5, supplement 2). Models that deliver less cargo ($c_i \approx d_i$) are less efficient in terms of cargo utilization, but have faster convergence. Achieving a convergence time roughly ten times faster required more than 90% of all cargo to remain in transit at steady state.

Distinct cell-type morphologies face order of magnitude differences in speed, precision and efficiency of trafficking

We wanted to see how these generic relationships between speed, precision and excess cargo affected global transport in different, realistic morphologies. We therefore implemented the families of sushi-belt models in representative morphologies from five cell types, spanning size and dendritic complexity (Fig. 6A). We simulated trafficking and delivery of cargo to a spatially uniform target distribution in each cell type to reveal morphology-dependent differences. In all cases we used optimistic estimates of transport kinetics, corresponding to a diffusion coefficient of 10 $\mu m^2 s^{-1}$.

Figure 6B shows spatial plots of the distribution of cargo on the microtubules (u_i, cyan-to-magenta colormap) and the distribution of delivered cargo ($u_i^\star$, black-to-orange colormap) for a model with an irreversible detachment rate of $8 \times 10^{-5}\ s^{-1}$. These parameters produce a relatively slow release of cargo — for each morphology, a sizable fraction of the cargo remains on the microtubules at ~3 hours, and it takes ~1-2 days to release all of the cargo (Supp. Fig. 2). While the speed of delivery is roughly equivalent, the accuracy varied across the neural morphologies. The hippocampal granule cell converged to very low error (~11.7% mean error), while the larger L5 pyramidal cell converged to ~27.7% error. The smaller, but more elaborately branched, Purkinje cell converged to a similarly high average error of ~29.1%.

As before, faster detachment rates produce faster, but less accurate, delivery; while slower detachment rates produce more accurate, but slower, delivery. These tradeoffs across the entire family of regimes are plotted in Fig. 6C (left). Adding a reattachment process largely preserved the effect of morphology on transport tradeoffs (Fig. 6C, right). We fixed the detachment rate to be fast (equally fast as trafficking between two 1 μm compartments), which is again an optimistic scenario. A tradeoff between excess cargo and speed of delivery emerged as the reattachment

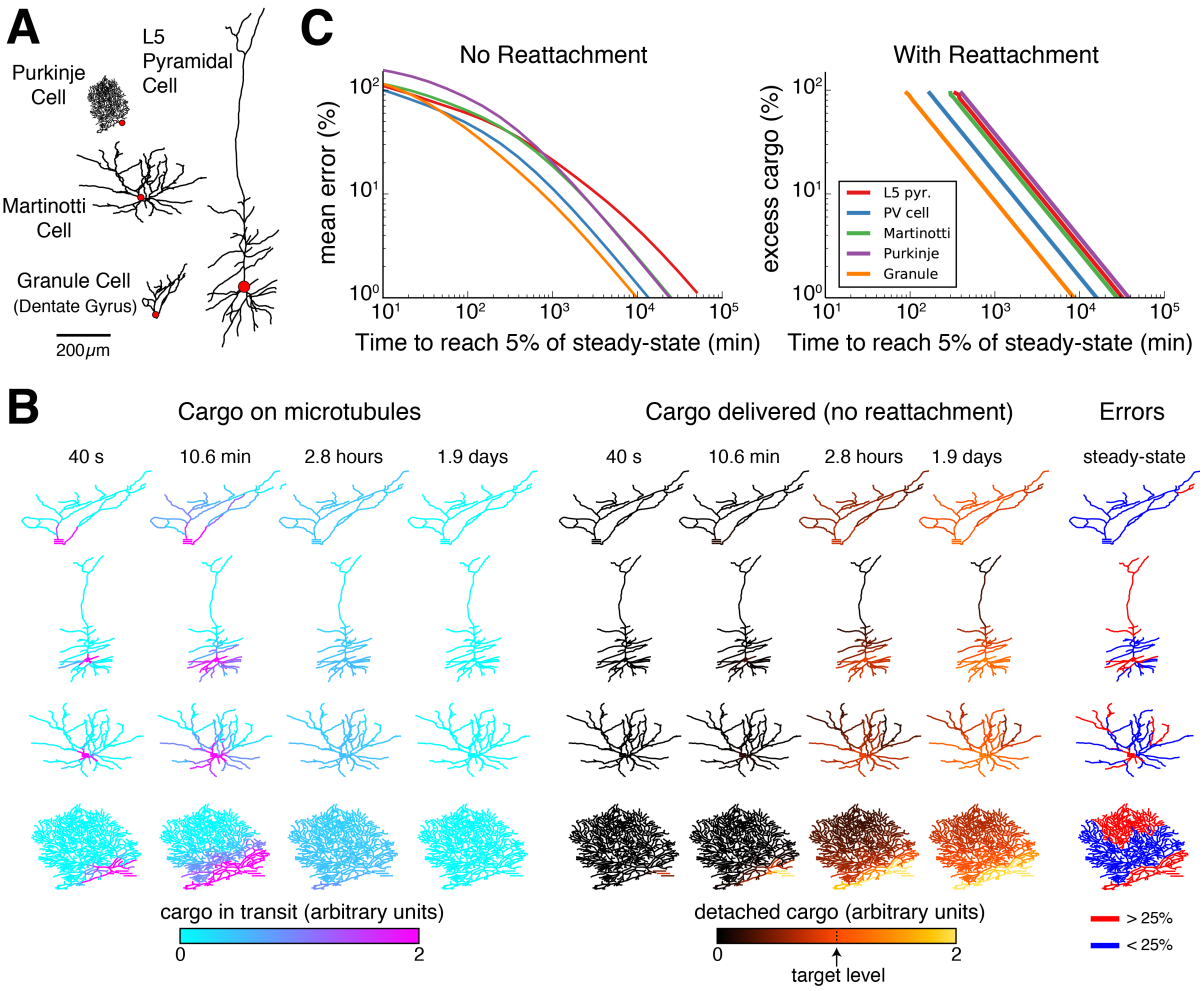

Figure 6. Effect of morphology on trafficking tradeoffs. **(A)** Representative morphologies from four neuron types, drawn to scale. The red dot denotes the position of the soma (not to scale). **(B)** Distribution of cargo on the microtubles (u_i) and delivered cargo ($u_i^\star$) at four time points for sushi-belt model with irreversible detachment. Cargo originated in the soma and was transported to a uniform distribution (all $a_i = b_i$, normalized to a diffusion coefficient of 10 μm^2 / s); the detachment rate was spatially uniform and equal to $8 \times 10^{-5} s^{-1}$. **(C)** Tradeoff curves for achieving a uniform distribution of cargo in realistic morphologies. The sushi-belt model without reattachment (as introduced in Fig. 4) suffers a tradeoff in speed and accuracy, while including reattachment (as in Fig. 7) produces a similar tradeoff between speed and excess "left-over" cargo. An optimistic diffusion coefficient of 10 $\mu m^2 s^{-1}$ was used in both cases. For simulations with reattachment, the detachment rate (c_i) was set equal to trafficking rates (a_i, b_i) for a 1 micron compartment. The detachment rate was increased linearly in proportion to compartment length in order to model a spatially uniform capture process.

rate was varied (Fig. 6C, right) and were most severe for the Purkinje cell and L5 pyramidal cell, and least severe for the Granule cell. Morphology itself therefore influences the relationship between delivery speed and precision, and/or excess cargo required, suggesting that different cell types might exploit different trafficking strategies.

DISCUSSION

The molecular motors that drive intracellular transport are remarkably efficient, achieving speeds of approximately 15 μm per minute (Rogers and Gelfand, 1998; Dynes and Steward, 2007; Müller et al., 2008). A naïve calculation based on this figure might suggest that subcellular cargo can be delivered within a few hours in most dendritic trees. However, this ignores the stochastic nature of biochemical processes — motors spontaneously change directions and cargo can be randomly delivered to the wrong site. Such chance events are inevitable in molecular systems, and in the case of active transport they lead to diffusion of bulk cargo in addition to directed movement. If this kind of biochemical stochasticity played out in the sushi restaurant analogy, then the waiting time for a dish wouldn't simply equate to the time taken for the chef to prepare the dish and for the belt to convey it. Instead, the restaurant would be beleaguered by fickle customers who pick up dishes they do not want, either withholding them for an indefinite period, or setting them on another belt destined for the kitchen.

Mathematical models provide a rigorous framework to test the plausibility and inherent relationships in conceptual models. Our study formalized the foremost conceptual model of dendritic transport (Doyle and Kiebler, 2011) to account for trafficking in realistic dendritic morphologies. Over a wide range of assumptions the model exhibits inherent and surprisingly punishing trade-offs between the accuracy of cargo delivery and the time taken to transport it over these morphologies. Using conservative estimates based on experimental data, the canonical sushi-belt model predicts delays of many hours or even days to match demand within 10%. Producing excess cargo and permitting reversible detachment from the microtubules can mitigate this tradeoff, but at substantial metabolic cost, since a large amount of excess cargo is required.

These predictions are unsettling, because nucleus-to-synapse transport appears to play a role in time-critical processes. Elevated synaptic activity can initiate distal metabolic events including transcription (Kandel, 2001; Deisseroth et al., 2003; Greer and Greenberg, 2008; Ch'ng and Martin, 2011) and this has been shown to be an important mechanism of neuronal plasticity (Nguyen et al., 1994; Frey and Morris, 1997, 1998; Bading, 2000; Kandel, 2001; Redondo and Morris, 2011). Moreover, neuronal activity has been observed to influence trafficking directly through second-messengers (Mironov, 2007; Wang and Schwarz, 2009; Soundararajan and Bullock, 2014), consistent with the hypothesis that trafficking rates are locally controlled. Genes that are transcribed in response to elevated activity can regulate synaptic strengths (Flavell and Greenberg, 2008; Bloodgood et al., 2013; Spiegel et al., 2014), and it has recently been suggested that nucleus-to-synapse trafficking of Arc directly regulates synaptic plasticity (Okuno et al., 2012). None of these findings imply that all kinds of molecular cargo are transported from the soma to distal dendritic locations, since mRNA can be sequestered and locally synthesized within dendrites (Kang and Schuman, 1996; Cajigas et al., 2012; Holt and Schuman, 2013). However, the speed, precision and efficiency tradeoffs revealed in the sushi belt model provide a principled way to understand why some processes might require local biosynthesis, while others operate globally.

The different ways that local demand signals can influence trafficking and detachment can impact global performance, sometimes non-intuitively. Many of these effects should be experimentally testable. For example, transport bottlenecks can be induced if demand signals target local trafficking rates along microtubules (the DDT model). Transport to distal compartments will be substantially faster when proximal demand is introduced (see Fig. 3). On the other hand, uniform trafficking combined with locally controlled detachment (DDD model, Fig. 4D) can avoid bottlenecks, and often leads to faster transport. However, this is not always the case, as was shown in figure 5D, where uniform trafficking is slower/inaccurate because cargo explores the basal dendritic tree even though

there is no demand in that region. Spatial tuning of trafficking speed permitted more efficient cargo delivery in the model. However, this has yet to be observed experimentally and would require extremely stereotyped morphology and physiological needs for it to be effective.

Intuitively, speed/precision/excess cargo tradeoffs arise because there is a conflict between exploring the dendritic tree for dropoff locations, capturing cargo in its current position and making sufficient excess cargo available to buffer local availability. For irreversible cargo detachment, the capture rate needs to be roughly an order of magnitude slower than trafficking, otherwise, compartments proximal to the soma receive disproportionately high levels of cargo. This scaling is unfavorable for achieving high accuracy: if it takes roughly 100 minutes to distribute cargo throughout the dendrites, it will take roughly 1000 minutes (16-17 hours) before the cargo dissociates and is delivered to the synapses. If, instead, cargo is able to reattach, then fast reattachment favors exploration at the cost of greater excess (i.e. non-utilized) cargo, while slow reattachment hinders transport, since more cargo is detached and thus immobile. Even when the vast majority of cargo is produced as excess, global delivery times of several hours persist. Furthermore, if a neuron needs to rapidly replace a cargo that is already present in high concentrations, the strategy of generating excess cargo will result in large dilution times.

Overall, our results show that there are multiple ways that neurons can distribute cargo, but each differs in its speed, accuracy and metabolic cost. Therefore, optimizing for any one of these properties comes at the expense of the others. For example, in the model without reattachment (Fig. 4), the same distribution of cargo can be achieved by: (a) location-dependent trafficking followed by uniform release, (b) uniform trafficking followed by location-dependent release, or (c) a mixture of these two strategies. Experimental findings appear to span these possibilities. Kim and Martin (2015) identified three mRNAs that were uniformly distributed in cultured *Aplysia* sensory neurons, but were targeted to synapses at the level of protein expression by localized translation (supporting option *b*). In contrast, the expression of *Arc* mRNA is closely matched to the pattern of Arc protein in granule cells of the dentate gyrus (possibly supporting option *a*; Steward et al., 1998; Farris et al., 2014; Steward et al., 2015). Trafficking kinetics do not just differ according to cargo identity — the same type of molecular cargo can exhibit diverse movement statistics in single-particle tracking experiments (Dynes and Steward, 2007). These differences lead us to speculate that different neuron types and different cargoes have adapted trafficking strategies that match performance tradeoffs to biological needs.

It is possible that active transport in biological neurons will be more efficient and flexible than models predict. For this reason, it is crucial to explore, quantitatively, the behavior of existing conceptual models by replacing words with equations so that we can see where discrepancies with biology might arise. More generally, conceptual models of subcellular processes deserve more quantitative attention because they can reveal non-obvious constraints, relationships and connections to other biological and physical phenomena (Smith and Simmons, 2001; Bressloff, 2006; Fedotov and Méndez, 2008; Newby and Bressloff, 2010b; Bhalla, 2011; Bressloff and Newby, 2013; Bhalla, 2014). Other modeling studies have focused on the effects of stochasticity and local trapping of cargo on a microscopic scale, particularly in the setting of low particle numbers (Bressloff, 2006; Bressloff and Earnshaw, 2007; Fedotov and Méndez, 2008; Newby and Bressloff, 2010b; Bressloff and Newby, 2013). We opted for a coarse-grained class of models in order to examine transport and delivery across an entire neuron. The model we used is necessarily an approximation: we assumed that cargo can be described as a concentration and that the multiple steps involved in cellular transport can lumped together in a mass action model.

By constraining trafficking parameters based on prior experimental measurements, we revealed physiologically

important tradeoffs across a variety of assumptions. It is an open and crucial question whether these modeling predictions hold biologically. Experimental falsification would prompt revision of the underlying models as well as our conceptual understanding of intracellular transport. On the other hand, experimental confirmation of these tradeoffs would have fundamental consequences for theories of synaptic plasticity and other physiological processes that are thought to require efficient nucleus-to-synapse trafficking.

METHODS

All simulation code is available online: https://github.com/ahwillia/Williams-etal-Synaptic-Transport

Model of single-particle transport

Let x_n denote the position of a particle along a 1-dimensional cable at timestep n. Let v_n denote the velocity of the particle at timestep n; for simplicity, we assume the velocity can take on three discrete values, $v_n = \{-1, 0, 1\}$, corresponding to a retrograde movement, pause, or anterograde movement. As a result, x_n is constrained to take on integer values. In the memoryless transport model (top plots in Fig. 1B, 1D, and 1F), we assume that v_n is drawn with fixed probabilities on each step. The update rule for position is:

$$x_{n+1} = x_n + v_n$$

$$v_{n+1} = \begin{cases} -1 & \text{with probability } p_- \\ 0 & \text{with probability } p_0 \\ 1 & \text{with probability } p_+ \end{cases}$$

We chose $p_- = 0.2$, $p_0 = 0.35$ and $p_+ = 0.45$ for the illustration shown in Figure 1. For the model with history-dependence (bottom plots in Fig. 1B, 1D, and 1F), the movement probabilities at each step depend on the previous movement. For example, if the motor was moving in an anterograde direction on the previous timestep, then it is more likely to continue to moving in that direction in the next time step. In this case the update rule is written in terms of conditional probabilities:

$$v_{n+1} = \begin{cases} -1 & \text{with probability } p(-|v_n) \\ 0 & \text{with probability } p(0|v_n) \\ 1 & \text{with probability } p(+|v_n) \end{cases}$$

In the limiting (non-stochastic) case of history-dependence, the particle always steps in the same direction as the previous time step.

	$v_n = -1$	$v_n = 0$	$v_n = 1$
$p(v_{n+1} = -1)$	1	0	0
$p(v_{n+1} = 0)$	0	1	0
$p(v_{n+1} = 1)$	0	0	1

We introduce a parameter $k \in [0,1]$ to linearly interpolate between this extreme case and the memoryless model.

	$v_n = -1$	$v_n = 0$	$v_n = 1$
$p(v_{n+1} = -1)$	$p_-(1-k)+k$	$p_-(1-k)$	$p_-(1-k)$
$p(v_{n+1} = 0)$	$p_0(1-k)$	$p_0(1-k)+k$	$p_0(1-k)$
$p(v_{n+1} = 1)$	$p_+(1-k)$	$p_+(1-k)$	$p_+(1-k)+k$

(7)

The bottom plots of figure 1B, 1D were simulated with $k = 0.5$.

To estimate the concentration and spatial distribution of cargo in real units, we used a 1 μm/$s$particle velocity and a 1 second time step to match experimental estimates of kinesin (Klumpp and Lipowsky, 2005, and references). We assumed a dendritic diameter of 7.2705 μm.

Relationship of single-particle transport to the mass-action model

The mass-action model (equation 1, in the *Results*) simulates the bulk movement of cargo across discrete compartments. Cargo transfer is modeled as an elementary chemical reaction obeying mass-action kinetics (Keener and Sneyd, 1998). For an unbranched cable, the change in cargo in compartment i is given by:

$$\dot{u}_i = a u_{i-1} + b u_{i+1} - (a+b) u_i \tag{8}$$

For now, we assume that the anterograde and retrograde trafficking rate constants (a and b, respectively) are spatially uniform.

The mass-action model can be related to a drift-diffusion partial differential equation (Fig. 1E) by discretizing u into spatial compartments of size Δ and expanding around some position, x:

$$\dot{u}(x) \approx a\left[u(x) - \Delta\frac{\partial u}{\partial x} + \frac{\Delta^2}{2}\frac{\partial^2 u}{\partial x^2}\right] + b\left[u(x) + \Delta\frac{\partial u}{\partial x} + \frac{\Delta^2}{2}\frac{\partial^2 u}{\partial x^2}\right] - (a+b)\,u(x) \tag{9}$$

$$= a\left[-\Delta\frac{\partial u}{\partial x} + \frac{\Delta^2}{2}\frac{\partial^2 u}{\partial x^2}\right] + b\left[\Delta\frac{\partial u}{\partial x} + \frac{\Delta^2}{2}\frac{\partial^2 u}{\partial x^2}\right] \tag{10}$$

We keep terms to second order in Δ, as these are of order dt in the limit $\Delta \to 0$ (Gardiner, 2009). This leads to a drift-diffusion equation:

$$\dot{u}(x) = \frac{\partial u}{\partial t} = \underbrace{(b-a)}_{\text{drift coefficient}}\frac{\partial u}{\partial x} + \underbrace{\left(\frac{a+b}{2}\right)}_{\text{diffusion coefficient}}\frac{\partial^2 u}{\partial x^2} \tag{11}$$

Measurements of the mean and mean-squared positions of particles in tracking experiments, or estimates of the average drift rate and dispersion rate of a pulse of labeled particles can thus provide estimates of parameters a and b.

How does this equation relate to the model of single-particle transport (Fig. 1A-B)? For a memoryless biased random walk, the expected position of a particle after n time steps is $E[x_n] = n(p_+ - p_-)$ and the variance in position after n steps is $n\left(p_+ + p_- - (p_+ - p_-)^2\right)$. For large numbers of non-interacting particles the mean and variance calculations for a single particle can be directly related to the ensemble statistics outlined above. We find:

$$a = \frac{2p_+ - (p_+ - p_-)^2}{2}$$

$$b = \frac{2p_- - (p_+ - p_-)^2}{2}$$

This analysis changes slightly when the single-particle trajectories contain long, unidirectional runs. The expected position for any particle is the same $E[x_n] = n(p_+ - p_-)$; the variance, in contrast, increases as run lengths increase. However, the mass-action model can often provide a good fit in this regime with appropriately re-fit parameters (see Fig. 1F). Introducing run lengths produces a larger effective diffusion coefficient and thus provides faster transport. As long as the single-particles have stochastic and identically distributed behavior, the ensemble will be well-described by a normal distribution by the central limit theorem. This only breaks down in the limit of very long unidirectional runs, as the system is no longer stochastic (Figure 1, Supplement 1).

Stochastic interpretation of the mass-action model

An important assumption of the mass-action model is that there are large numbers of transported particles, so that the behavior of the total system is deterministic. Intuitively, when each compartment contains many particles, then small fluctuations in particle number don't appreciably change concentration. Many types of dendritic cargo are present in high numbers (Cajigas et al., 2012).

When few cargo particles are present, fluctuations in particle number are more functionally significant. Although we did not model this regime directly, the mass-action model also provides insight into this stochastic regime. Instead of interpreting u_i as the amount of cargo in compartment i, this variable (when appropriately normalized) can be interpreted as the probability of a particle occupying compartment i. Thus, for a small number of transported cargoes, the mass-action model describes the average, or expected, distribution of the ensemble.

In this interpretation, the mass-action model models a spatial probability distribution. Let p_i denote the probability of a particle occupying compartment i. If a single particle starts in the somatic compartment at $t = 0$, and we query this particle's position after a long period of transport, then the probability ratio between of finding this particle in any parent-child pair of compartments converges to:

$$\left.\frac{p_p}{p_c}\right|_{ss} = \frac{b}{a}$$

which is analogous to equation (3) in the *Results*.

In the stochastic model, the number of molecules in each compartment converges to a binomial distribution at steady-state; the coefficient of variation in each compartment is given by:

$$\sqrt{\frac{1 - p_i^{(ss)}}{n\, p_i^{(ss)}}}$$

This suggests two ways of decreasing noise. First, increasing the total number of transported molecules, n, decreases the noise by a factor of $1/\sqrt{n}$. Second, increasing p_i decreases the noise in compartment i. However, this second option necessarily comes at the cost of decreasing occupation probability and thus increasing noise in other compartments.

Estimating parameters of the mass-action model using experimental data

The parameters of the mass-action model we study can be experimentally fit by estimating the drift and diffusion coefficients of particles over the length of a neurite. A common approach is to plot the mean displacement and mean squared displacement of particles as a function of time. The slopes of the best-fit lines in these cases respectively estimate the drift and diffusion coefficients in (11). Diffusion might not accurately model particle movements over short time scales because unidirectional cargo runs result in superdiffusive motion, evidenced by superlinear increases in mean squared-displacement with time (Caspi et al., 2000). However, over longer timescales, cargoes that stochastically change direction can be modeled as a diffusive process (Soundararajan and Bullock, 2014).

The mass-action model might also be fit by tracking the positions of a population of particles with photoactivatable GFP (Roy et al., 2012). In this case, the distribution of fluorescence at each point in time could be fit by a Gaussian distribution; the drift and diffusion coefficients are respectively proportional to the rate at which the estimated mean and variance evolves over time.

These experimental measurements can vary substantially across neuron types, experimental conditions, and cargo identities. Therefore, in order to understand fundamental features and constraints of the sushi belt model across systems, it is more useful to explore relationships within the model across ranges of parameters. Unless otherwise stated, the trafficking kinetics were constrained so that $a_i + b_i = 1$ for each pair of connected compartments. This is equivalent to having a constant diffusion coefficient of one across all compartments. Given a target expression pattern along the microtubules, this is the only free parameter of the trafficking simulations; increasing the diffusion coefficient will always shorten convergence times, but not qualitatively change our results. In figure 6 we fixed the diffusion coefficients as specified in the *Results* based on optimistic estimates (Caspi et al., 2000; Soundararajan and Bullock, 2014).

Steady-state analysis

The steady-state ratio of trafficked cargo in neighboring compartments equals the ratio of the trafficking rate constants (equation 2). Consider a unbranched neurite with non-uniform anterograde and retrograde rate constants (equation 1). It is easy to verify the steady-state relationship in the first two compartments, by setting $\dot{u}_1 = 0$ and solving:

$$-a_1 u_1 + b_1 u_2 = 0 \;\Rightarrow\; \left.\frac{u_1}{u_2}\right|_{ss} = \frac{b_1}{a_1}$$

Successively applying the same logic down the cable confirms the condition in equation 2 holds globally. The more general condition for branched morphologies can be proven by a similar procedure (starting at the tips and moving in).

It is helpful to re-express the mass-action trafficking model as a matrix differential equation, $\dot{\mathbf{u}} = A\mathbf{u}$, where $\mathbf{u} = [u_1, u_2, \ldots u_N]^T$ is the state vector, and A is the state-transition matrix. For a general branched morphology, A will be nearly tridiagonal, with off-diagonal elements corresponding to branch points; matrices in this form are called

Hines matrices (Hines, 1984). For the simpler case of an unbranched cable, A is tridiagonal:

$$A = \begin{bmatrix} -a_1 & b_1 & 0 & & \dots & 0 \\ a_1 & -b_1 - a_2 & b_2 & 0 & & \\ 0 & a_2 & -b_2 - a_3 & b_3 & \ddots & \vdots \\ \vdots & 0 & a_3 & \ddots & & 0 \\ & & \ddots & & -b_{N-2} - a_{N-1} & b_{N-1} \\ 0 & & \dots & 0 & a_{N-1} & -b_{N-1} \end{bmatrix}$$

For both branched and unbranched morphologies, each column of A sums to zero, which reflects conservation of mass within the system. Assuming nonzero trafficking rates, the rank of A is exactly $N-1$ (this can be seen by taking the sum of the first $N-1$ rows, which results in -1 times the final row). Thus, the nullspace of A is one-dimensional. Equation (3) describes this manifold of solutions: the level of cargo can be scaled by a common multiplier across all compartments without disrupting the relation in (2).

The steady-state distribution, $\tilde{\mathbf{u}}$, is a vector that spans the nullspace of A. It is simple to show that all other eigenvalues A are negative using the Gershgorin circle theorem; thus, the fixed point described by equation 2 is stable. The convergence rate is determined by the non-zero eigenvalue with smallest magnitude of A. There are no other fixed points or limit cycles in this system.

Biologically plausible model of a local demand signal

There are many biochemical mechanisms that could signal demand. Here we briefly explore cytosolic calcium, $[Ca]_i$, as a candidate mechanism since it is modulated by local synaptic activity and $[Ca]_i$ transients simultaneously arrest anterograde and retrograde microtubular transport for certain cargoes (Wang and Schwarz, 2009). We represent the effect of the calcium-dependent pathway by some function of calcium, $f([Ca_i])$. This function could, for example, capture the binding affinity of $[Ca]_i$ to enzymes that alter the kinetics of motor proteins; the Hill equation would provide a simple functional form. If all outgoing trafficking rates of a compartment are controlled by cytosolic calcium — i.e. for any parent-child pair of compartments we have $a = f([Ca]_p)$ and $b = f([Ca]_c)$ — then condition in equation 4 is satisfied:

$$\frac{b}{a} = \frac{f([Ca]_c)}{f([Ca]_p)} = \frac{\tilde{u}_p}{\tilde{u}_c} \tag{12}$$

where $\tilde{u}_i = 1/f([Ca]_i)$. We emphasize that other potential signaling pathways could achieve the same effect, so while there is direct evidence for $[Ca]_i$ as an important signal, the model can be interpreted broadly, with $[Ca]_i$ serving as a placeholder for any local signal identified experimentally. Further, $[Ca]_i$ itself may only serve as a demand signal over short timescales, while other, more permanent, signals such as microtubule-associated proteins (Soundararajan and Bullock, 2014) are needed to signal demand over longer timescales.

Simulations in realistic morphologies

We obtained a CA1 pyramidal cell model Migliore and Migliore (2012) from the online repository ModelDB (https://senselab.med.yale.edu/modeldb/), accession number 144541. We used the same spatial compartments used by Migliore and Migliore (2012) and set the trafficking and dissociation parameters of the mass-action transport model without reference to the geometry of the compartments. The mass-action model was simulated in Python

by solving matrix exponentials of A with the scipy library (Jones et al., 2001). In figure 2 we simulated electrical activity of this model with excitatory synaptic input for 5 seconds using the Python API to NEURON (Hines et al., 2009). We used the average membrane potential over this period to set the target demand level. In Figures 3 and 4, we imposed artificial demand profiles with regions of low-demand and high-demand (10x larger) as depicted in the figures.

In figure 8, we obtained representative morphologies of five cell types from neuromorpho.org (Ascoli et al., 2007). Specifically, we downloaded a Purkinje cell (`Purkinje-slice-ageP43-6`), a parvalbumin-positive interneuron (`AWa80213`), a Martinotti cell (`C100501A3`), a layer-5 pyramidal cell (`32-L5pyr-28`), and a granule cell from the dentate gyrus (`041015-vehicle1`). In these simulations, we scaled the trafficking parameters inversely proportional to the squared distance between the midpoints of the compartments. Doing this fixes the diffusion coefficient of cargo trafficking as a constant, Speci Δ For simulations with reattachment, we set the detachment rate (c_i) was set equal to trafficking rates (a_i, b_i) for a 1 micron compartment. The detachment rate was increased linearly in proportion to compartment length in order to model a spatially uniform capture process. We used a custom-written Python library to generate movies and figures for these simulations (Williams, 2016).

Incorporating detachment and reattachment into the mass-action model

Introducing detachment into the mass-action model. For compartment i in a cable, the differential equations become:

$$\begin{aligned} \dot{u}_i &= a_{i-1}u_{i-1} - (a_i + b_{i-1} + c_i)u_i + b_i u_{i+1} \\ \dot{u}_i^\star &= c_i u_i \end{aligned}$$

When $a_i, b_i \gg c_i$, then the distribution of cargo on the microtubules (u_i) approaches a quasi-steady-state that follows equation 3. In figure 4, we present DDT and DDD models as two strategies that distribute cargo to match a demand signal $\tilde{u}_i^\star$. As mentioned in the main text, a spectrum of models that interpolate between these extremes are possible. To interpolate between these strategies, let F be a scalar between 0 and 1, and let $\tilde{u}^\star$ be normalized to sum to one. We choose a_i and b_i to achieve:

$$\tilde{u}_i = F\ \tilde{u}_i^\star + (1-F)/N$$

along the microtubular network and choose c_i to satisfy

$$c_i \propto \frac{\tilde{u}_i^\star}{F\ \tilde{u}_i^\star + (1-F)/N}$$

. Here, N is the number of compartments in the model. Setting $F = 1$ results in the DDT model (demand is satisfied purely by demand-modulated trafficking, and non-specific detachment, Fig. 4C). Setting $F = 0$ results in the DDD model (demand is satisfied purely by demand-modulated detachment, and uniform/non-specific trafficking, Fig. 4D). An interpolated strategy is shown in figure 4E ($F = 0.3$).

The mass-action model with reattachment (equation 6) produces the following system of differential equations for a linear cable, with d_i denoting the rate constant of reattachment in compartment i

$$\begin{aligned} \dot{u}_i &= a_{i-1}u_{i-1} - (a_i + b_{i-1} + c_i)u_i + b_i u_{i+1} + d_i u_i^\star \\ \dot{u}_i^\star &= c_i u_i - d_i u_i^\star \end{aligned}$$

We examined the DDD model with $N = 100$ compartments and diffusion coefficient of $10\mu\text{m}^2\ \text{s}^{-1}$. The maximal detachment rate constant and the reattachment rates were tunable parameters, while the reattachment rates were spatially uniform. Results were similar when reattachment was modulated according to demand (data not shown, see supplemental simulations at https://github.com/ahwillia/Williams-etal-Synaptic-Transport).

Globally tuning transport rates to circumvent the speed-specificity tradeoff

In figure 5, supplement 1, we explored whether fine-tuning the trafficking rates could provide both fast and precise cargo distribution. We investigated the DDD model with fast detachment rates in an unbranched cable with equally spaced synapses and $N = 100$ compartments. Large detachment rates produced a proximal bias in cargo delivery which we empirically found could be corrected by setting the anterograde and retrograde trafficking rates to be:

$$a_i = \frac{D}{2} + \beta \cdot \frac{N-1-i}{N-2}$$

$$b_i = \frac{D}{2} - \beta \cdot \frac{N-1-i}{N-2}$$

where $i = \{1, 2, \ldots N-1\}$ indexes the trafficking rates from the soma ($i = 1$) to the other end of the cable ($i = N-1$), and $D = 10\mu\text{m}^2/\text{s}$ is the diffusion coefficient. Faster detachment rates require larger values for the parameter β; note that $\beta < D/2$ is a constraint to prevent b_i from becoming negative. This heuristic qualitatively improved, but did not precisely correct for, fast detachment rates in the DDT model (data not shown).

Intuitively, the profile of the proximal delivery bias is roughly exponential (Fig. 6B), and therefore the anterograde rates need to be tuned more aggressively near the soma (where the bias is most pronounced), and more gently tuned as the distance to the soma increases. Importantly, tuning the trafficking rates in this manner does not alter the diffusion coefficient (proportional to $a_i + b_i$) constant along the length of the cable. Instead, by increasing a_i and decreasing b_i we introduce a rightward drift/velocity in the cargo distribution.

ACKNOWLEDGEMENTS

We thank Eve Marder, Subhaneil Lahiri, Friedemann Zenke, and Benjamin Regner for useful feedback on the manuscript, and thank Simon Bullock for useful discussion. This research was supported by the Department of Energy Computational Science Graduate Fellowship, NIH Grant 1P01NS079419, NIH Grant P41GM103712, the Howard Hughes Medical Institute, and the Charles A. King Trust.

COMPETING INTERESTS

The authors declare that there are no competing interests.

REFERENCES

Aakalu, G., Smith, W. B., Nguyen, N., Jiang, C., and Schuman, E. M. (2001). Dynamic visualization of local protein synthesis in hippocampal neurons. *Neuron*, 30(2):489–502.

Ascoli, G. A., Donohue, D. E., and Halavi, M. (2007). Neuromorpho. org: a central resource for neuronal morphologies. *J. Neurosci.*, 27(35):9247–9251.

Bading, H. (2000). Transcription-dependent neuronal plasticity. *Eur. J. Biochem.*, 267(17):5280–5283.

Bhalla, U. S. (2011). Trafficking Motifs as the Basis for Two-Compartment Signaling Systems to Form Multiple Stable States. *Biophys. J.*, 101(1):21–32.

Bhalla, U. S. (2014). Molecular computation in neurons: a modeling perspective. *Curr. Opin. Neurobiol.*, 25:31–37.

Block, S. M., Goldstein, L. S. B., and Schnapp, B. J. (1990). Bead movement by single kinesin molecules studied with optical tweezers. *Nature*, 348(6299):348–352.

Bloodgood, B. L., Sharma, N., Browne, H. A., Trepman, A. Z., and Greenberg, M. E. (2013). The activity-dependent transcription factor npas4 regulates domain-specific inhibition. *Nature*, 503(7474):121–125.

Bressloff, P. and Earnshaw, B. (2007). Diffusion-trapping model of receptor trafficking in dendrites. *Phys. Rev. E*, 75(4):041915.

Bressloff, P. and Newby, J. (2009). Directed intermittent search for hidden targets. *New J. Phys.*, 11(2):023033.

Bressloff, P. C. (2006). Stochastic model of protein receptor trafficking prior to synaptogenesis. *Phys. Rev. E Stat. Nonlin. Soft. Matter. Phys.*, 74(3).

Bressloff, P. C. and Newby, J. M. (2013). Stochastic models of intracellular transport. *Rev. Mod. Phys.*, 85(1):135–196.

Buxbaum, A. R., Haimovich, G., and Singer, R. H. (2014a). In the right place at the right time: visualizing and understanding mRNA localization. *Nat. Rev. Mol. Cell Biol.*, 16(2):95–109.

Buxbaum, A. R., Wu, B., and Singer, R. H. (2014b). Single-Actin mRNA Detection in Neurons Reveals a Mechanism for Regulating Its Translatability. *Science*, 343(6169):419–422.

Buxbaum, A. R., Yoon, Y. J., Singer, R. H., and Park, H. Y. (2015). Single-molecule insights into mRNA dynamics in neurons. *Trends Cell Biol.*, 25(8):468–475.

Cajigas, I. J., Tushev, G., Will, T. J., tom Dieck, S., Fuerst, N., and Schuman, E. M. (2012). The local transcriptome in the synaptic neuropil revealed by deep sequencing and high-resolution imaging. *Neuron*, 74(3):453–466.

Caspi, A., Granek, R., and Elbaum, M. (2000). Enhanced diffusion in active intracellular transport. *Phys. Rev. Lett.*, 85:5655–5658.

Ch'ng, T. and Martin, K. (2011). Synapse-to-nucleus signaling. *Curr. Opin. Neurobiol.*, 21:345–52.

Deisseroth, K., Mermelstein, P. G., Xia, H., and Tsien, R. W. (2003). Signaling from synapse to nucleus: the logic behind the mechanisms. *Curr. Opin. Neurobiol.*, 13(3):354–365.

Doyle, M. and Kiebler, M. A. (2011). Mechanisms of dendritic mRNA transport and its role in synaptic tagging. *EMBO J.*, 30(17):3540–3552.

Dynes, J. L. and Steward, O. (2007). Dynamics of bidirectional transport of *Arc* mRNA in neuronal dendrites. *J. Comp. Neurol.*, 500(3):433–447.

Farris, S., Lewandowski, G., Cox, C. D., and Steward, O. (2014). Selective Localization of *Arc* mRNA in Dendrites Involves Activity- and Translation-Dependent mRNA Degradation. *J. Neurosci.*, 34(13):4481–4493.

Fedotov, S. and Méndez, V. (2008). Non-markovian model for transport and reactions of particles in spiny dendrites. *Phys. Rev. Lett.*, 101(21):218102.

Flavell, S. W. and Greenberg, M. E. (2008). Signaling mechanisms linking neuronal activity to gene expression and plasticity of the nervous system. *Annual review of neuroscience*, 31:563.

Frey, U. and Morris, R. (1998). Weak before strong: dissociating synaptic tagging and plasticity-factor accounts of late-LTP. *Neuropharmacol.*, 37(4-5):545–552.

Frey, U. and Morris, R. G. M. (1997). Synaptic tagging and long-term potentiation. *Nature*, 385(6616):533–536.

Gagnon, J. and Mowry, K. (2011). Molecular motors: directing traffic during RNA localization. *Crit Rev Biochem Mol Biol*, 46:229–39.

Gardiner, C. (2009). *Stochastic Methods: A Handbook for the Natural and Social Sciences (Springer Series in Synergetics)*. Springer, 4 edition.

Grant, B. D. and Donaldson, J. G. (2009). Pathways and mechanisms of endocytic recycling. *Nat. Rev. Mol. Cell Biol.*, 10(9):597–608.

Greer, P. L. and Greenberg, M. E. (2008). From synapse to nucleus: Calcium-dependent gene transcription in the control of synapse development and function. *Neuron*, 59(6):846 – 860.

Han, E. B. and Heinemann, S. F. (2013). Distal Dendritic Inputs Control Neuronal Activity by Heterosynaptic Potentiation of Proximal Inputs. *J. Neurosci.*, 33(4):1314–1325.

Hancock, W. O. (2014). Bidirectional cargo transport: moving beyond tug of war. *Nat. Rev. Mol. Cell Biol.*, 15(9):615–628.

Hines, M. (1984). Efficient computation of branched nerve equations. *Int. J. Biomed. Comput.*, 15(1):69–76.

Hines, M. L., Davison, A. P., and Muller, E. (2009). Neuron and python. *Front. Neuroinform.*, 3.

Hirokawa, N., Niwa, S., and Tanaka, Y. (2010). Molecular Motors in Neurons: Transport Mechanisms and Roles in Brain Function Development, and Disease. *Neuron*, 68(4):610–638.

Hoffman, D., Magee, J., Colbert, C., and Johnston, D. (1997). K^+ channel regulation of signal propagation in dendrites of hippocampal pyramidal neurons. *Nature*, 387:869–75.

Holt, C. E. and Schuman, E. M. (2013). The central dogma decentralized: New perspectives on RNA function and local translation in neurons. *Neuron*, 80(3):648–657.

Jones, E., Oliphant, T., Peterson, P., et al. (2001). SciPy: Open source scientific tools for Python.

Kandel, E. R. (2001). The Molecular Biology of Memory Storage: A Dialogue Between Genes and Synapses. *Science*, 294(5544):1030–1038.

Kang, H. and Schuman, E. M. (1996). A requirement for local protein synthesis in neurotrophin-induced hippocampal synaptic plasticity. *Science*, 273(5280):1402–1406.

Kao, D.-I., Aldridge, G. M., Weiler, I. J., and Greenough, W. T. (2010). Altered mRNA transport, docking, and protein translation in neurons lacking fragile x mental retardation protein. *Proc. Natl. Acad. Sci. USA*, 107(35):15601–15606.

Keener, J. P. and Sneyd, J. (1998). *Mathematical Physiology*. Springer, New York.

Kim, S. and Martin, K. C. (2015). Neuron-wide RNA transport combines with netrin-mediated local translation to spatially regulate the synaptic proteome. *eLife*, 4:e04158.

Klumpp, S. and Lipowsky, R. (2005). Cooperative cargo transport by several molecular motors. *Proc. Natl. Acad. Sci. U.S.A.*, 102(48):17284–17289.

Lyles, V., Zhao, Y., and Martin, K. C. (2006). Synapse Formation and mRNA Localization in Cultured Aplysia Neurons. *Neuron*, 49(3):349–356.

Magee, J. (1998). Dendritic hyperpolarization-activated currents modify the integrative properties of hippocampal CA1 pyramidal neurons. *J Neurosci*, 18:7613–24.

Migliore, M. and Migliore, R. (2012). Know your current I_h: Interaction with a shunting current explains the puzzling effects of its pharmacological or pathological modulations. *PLoS ONE*, 7(5):e36867.

Mironov, S. L. (2007). ADP Regulates Movements of Mitochondria in Neurons. *Biophys. J.*, 92(8):2944–2952.

Moga, D., Calhoun, M., Chowdhury, A., Worley, P., Morrison, J., and Shapiro, M. (2004). Activity-regulated cytoskeletal-associated protein is localized to recently activated excitatory synapses. *Neurosci.*, 125(1):7–11.

Müller, M. J. I., Klumpp, S., and Lipowsky, R. (2008). Tug-of-war as a cooperative mechanism for bidirectional cargo transport by molecular motors. *Proc. Natl. Acad. Sci. U.S.A.*, 105(12):4609–4614.

Newby, J. and Bressloff, P. C. (2010a). Local synaptic signaling enhances the stochastic transport of motor-driven cargo in neurons. *Phys. Biol.*, 7(3):036004.

Newby, J. M. and Bressloff, P. C. (2010b). Quasi-steady state reduction of molecular motor-based models of directed intermittent search. *B. Math. Biol.*, 72(7):1840–1866.

Nguyen, P. V., Abel, T., and Kandel, E. R. (1994). Requirement of a critical period of transcription for induction of a late phase of LTP. *Science*, 265(5175):1104–1107.

Okuno, H., Akashi, K., Ishii, Y., Yagishita-Kyo, N., Suzuki, K., Nonaka, M., Kawashima, T., Fujii, H., Takemoto-Kimura, S., Abe, M., Natsume, R., Chowdhury, S., Sakimura, K., Worley, P. F., and Bito, H. (2012). Inverse Synaptic Tagging of Inactive Synapses via Dynamic Interaction of Arc/Arg3.1 with CaMKIIβ. *Cell*, 149(4):886 – 898.

Park, M., Penick, E. C., Edwards, J. G., Kauer, J. A., and Ehlers, M. D. (2004). Recycling endosomes supply AMPA receptors for LTP. *Science*, 305(5692):1972–1975.

Park, M., Salgado, J. M., Ostroff, L., Helton, T. D., Robinson, C. G., Harris, K. M., and Ehlers, M. D. (2006). Plasticity-induced growth of dendritic spines by exocytic trafficking from recycling endosomes. *Neuron*, 52(5):817–830.

Redondo, R. L. and Morris, R. G. (2011). Making memories last: the synaptic tagging and capture hypothesis. *Nat. Rev. Neurosci.*, 12(1):17–30.

Rogers, S. L. and Gelfand, V. I. (1998). Myosin cooperates with microtubule motors during organelle transport in melanophores. *Curr. Biol.*, 8(3):161–164.

Roy, S., Yang, G., Tang, Y., and Scott, D. A. (2012). A simple photoactivation and image analysis module for visualizing and analyzing axonal transport with high temporal resolution. *Nat. Protoc.*, 7(1):62–68.

Smith, D. and Simmons, R. (2001). Models of Motor-Assisted Transport of Intracellular Particles. *Biophys. J.*, 80(1):45–68.

Soundararajan, H. C. and Bullock, S. L. (2014). The influence of dynein processivity control, maps, and microtubule ends on directional movement of a localising mRNA. *eLife*, 3:e01596.

Spiegel, I., Mardinly, A. R., Gabel, H. W., Bazinet, J. E., Couch, C. H., Tzeng, C. P., Harmin, D. A., and Greenberg, M. E. (2014). Npas4 regulates excitatory-inhibitory balance within neural circuits through cell-type-specific gene programs. *Cell*, 157(5):1216 – 1229.

Steward, O., Farris, S., Pirbhoy, P. S., Darnell, J., and Driesche, S. J. V. (2015). Localization and local translation of *Arc/Arg3.1* mRNA at synapses: some observations and paradoxes. *Front. Mol. Neurosci.*, 7.

Steward, O., Wallace, C., Lyford, G., and Worley, P. (1998). Synaptic Activation Causes the mRNA for the IEG *Arc* to Localize Selectively near Activated Postsynaptic Sites on Dendrites. *Neuron*, 21(4):741–751.

Steward, O. and Worley, P. F. (2001). Selective Targeting of Newly Synthesized *Arc* mRNA to Active Synapses Requires NMDA Receptor Activation. *Neuron*, 30(1):227–240.

Sutton, M. A. and Schuman, E. M. (2006). Dendritic protein synthesis, synaptic plasticity, and memory. *Cell*, 127(1):49–58

643 Vickers, C. A., Dickson, K. S., and Wyllie, D. J. A. (2005). Induction and maintenance of late-phase long-term
644 potentiation in isolated dendrites of rat hippocampal CA1 pyramidal neurones. *J. Physiol.*, 568(3):803–813.
645 Voit, E. O., Martens, H. A., and Omholt, S. W. (2015). 150 years of the mass action law. *PLoS Comput. Biol.*,
646 11(1):1–7.
647 Wang, X. and Schwarz, T. L. (2009). The Mechanism of Ca^{2+}-Dependent Regulation of Kinesin-Mediated
648 Mitochondrial Motility. *Cell*, 136(1):163–174.
649 Welte, M. A. (2004). Bidirectional transport along microtubules. *Curr. Biol.*, 14(13):R525–R537.
650 Williams, A. H. (2016). PyNeuron Toolbox. https://github.com/ahwillia/PyNeuron-Toolbox.
651 Wu, B., Eliscovich, C., Yoon, Y. J., and Singer, R. H. (2016). Translation dynamics of single mRNAs in live cells
652 and neurons. *Science*, 352(6292):1430–1435.
653 Zheng, N., Jeyifous, O., Munro, C., Montgomery, J. M., and Green, W. N. (2015). Synaptic activity regulates AMPA
654 receptor trafficking through different recycling pathways. *eLife*, 4.

FIGURE SUPPLEMENTS

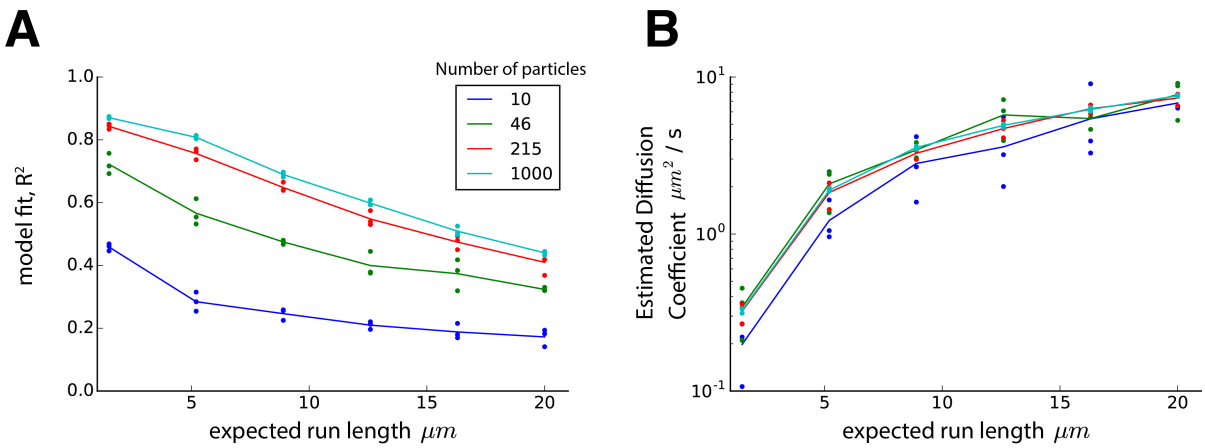

Figure 1 supplement 1. The effect of cargo run length on mass-action model fit and diffusion coefficient. The model of stochastic particle movement (Equation 7, *Methods*) was simulated with equal transition probabilities ($p_- = p_0 = p_+ = 1/3$) for various values of k and particle numbers in an infinite cable with 1 μm compartments and 1 second time steps. The expected run length is given by the mean of a negative binomial distribution. For each simulation, a mass-action approximation was fit by matching the first two moments of the cargo distribution, as described in the *Methods*. In both panels, dots represent simulated triplicates, and lines denote the average outcome with colors denoting the simulated ensemble size (see legend). **(A)** The mass-action model (Equation 1, *Results*) provides a reasonably accurate fit after 100 seconds of simulation with moderately long run lengths and low particle numbers. The fit improves for longer simulations and larger particle numbers, since the cargo distribution is better approximated by a normal distribution under these conditions due to the central limit theorem. The coefficient of determination, R^2, reflects the proportion of explained variance by the mass-action model (equivalent to a Gaussian fit to the concentration profile). **(B)** The estimated diffusion coefficient of the mass-action model (i.e. the variance of the Gaussian fit in panel A) increases as expected run length increases.

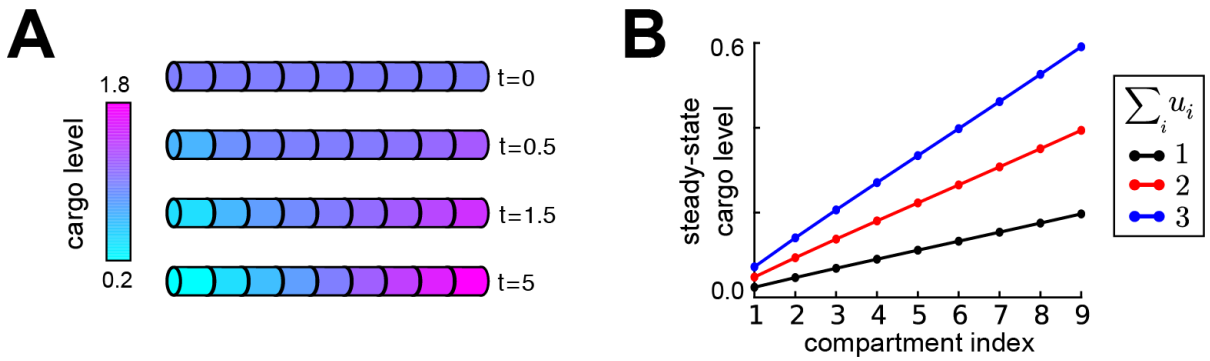

Figure 2 supplement 1. Equation 4 specifies the relative distribution of cargo, changing the total amount of cargo scales this distribution. **(A)** Inspired by ion channel expression gradients observed in hippocampal cells(Hoffman et al., 1997; Magee, 1998), we produced a linear gradient in cargo distribution in an unbranched cable. By equation 4, the trafficking rate constants satisfy $b_i/a_i = i/i+1$ (where i indexes on increasing distance to the soma). Starting from a uniform distribution of cargo in the cable ($t = 0$ a.u.), the desired linear profile emerges over time. **(B)** Changing the amount of cargo in the cable (the sum of u_i across all compartments, see legend) does not disrupt the steady-state linear expression profile, but scales its slope.

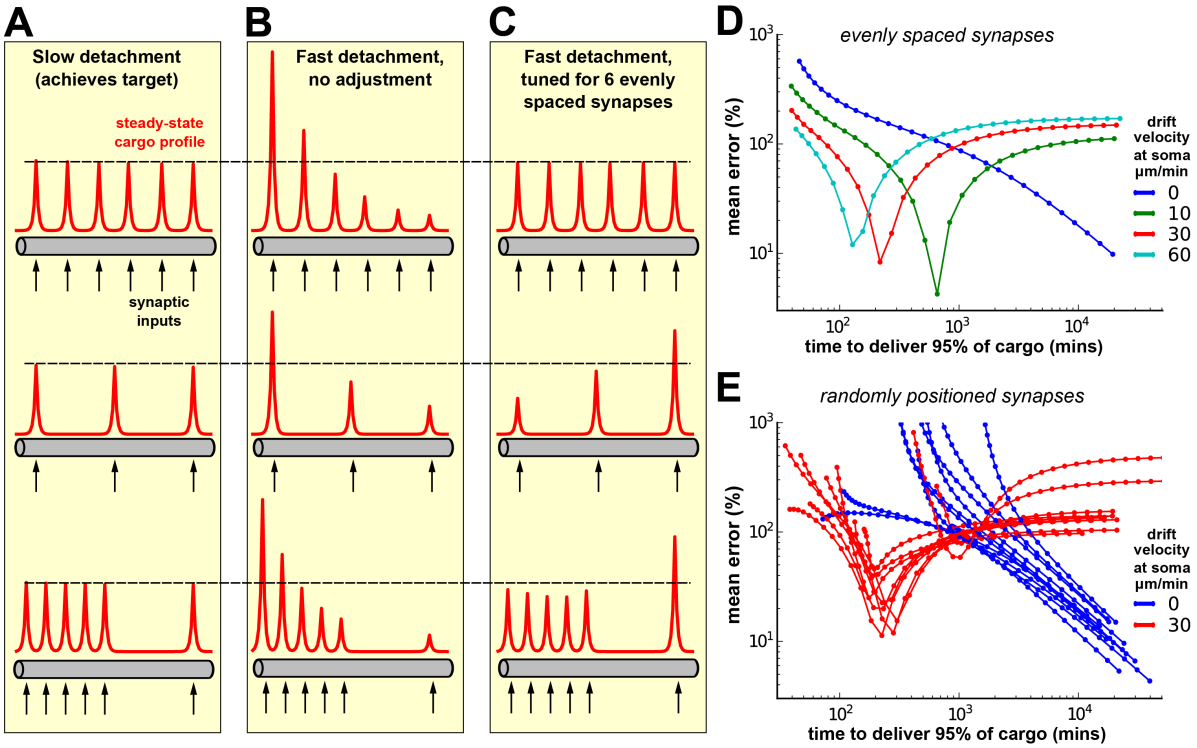

Figure 5 supplement 1. Tuning the model for speed and specificity results in sensitivity to the target spatial distribution of cargo. **(A-C)** Cargo begins on the left end of an unbranched cable, and is ideally distributed equally amongst a number recently stimulated synaptic sites (black arrows). We set the length of the cable to 800 μm (roughly the length of an apical dendrite in a CA1 cell) and the diffusion coefficient to 10 μm^2/s — an estimate on the upper end of what might be biologically achieved (see Fig. 1, Caspi et al., 2000; Soundararajan and Bullock, 2014). Steady-state cargo profiles (red) for three stimulation patterns (black arrows) along an unbranched cable. The dotted black line corresponds to the 'target' steady-state level at each delivery site. **(A)** When the timescale of detachment is sufficiently slow, cargo can be evenly distributed to the synapses regardless of their number and position. Transport parameters were set according to the procedure shown in figure 4D. **(B)** When detachment is näively increased (all rates multiplicatively scaled) a proximal bias in the steady-state distribution of cargo across all stimulation patterns. **(C)** Transport rate constants, a_i and b_i, were tuned to optimize the distribution of cargo to six equally spaced synapses (top row); detachment rate constants were the same as in panel B. Changing the number of synapses (middle row) or the position of the synapses (bottom row) causes the unequal distribution of cargo to synapses. **(D)** Tradeoff curves between non-specificity and convergence rate for six evenly spaced synapses (top row of A-C). Trafficking parameters were chosen so that the anterograde velocity decreased linearly over the length of the cable; the color of the lines shows the maximum velocity at the soma. The tradeoff curves shift to the left and becomes non-monotonic as the anterograde velocity increases. **(E)** Tradeoff curves for six randomly positioned synapses drawn uniformly across the cable. Ten simulations are shown for two levels of anterograde velocity (blue lines, 0 μm/min; red lines 30 μm/min); as before, the velocity linearly decreased across the length of the cable.

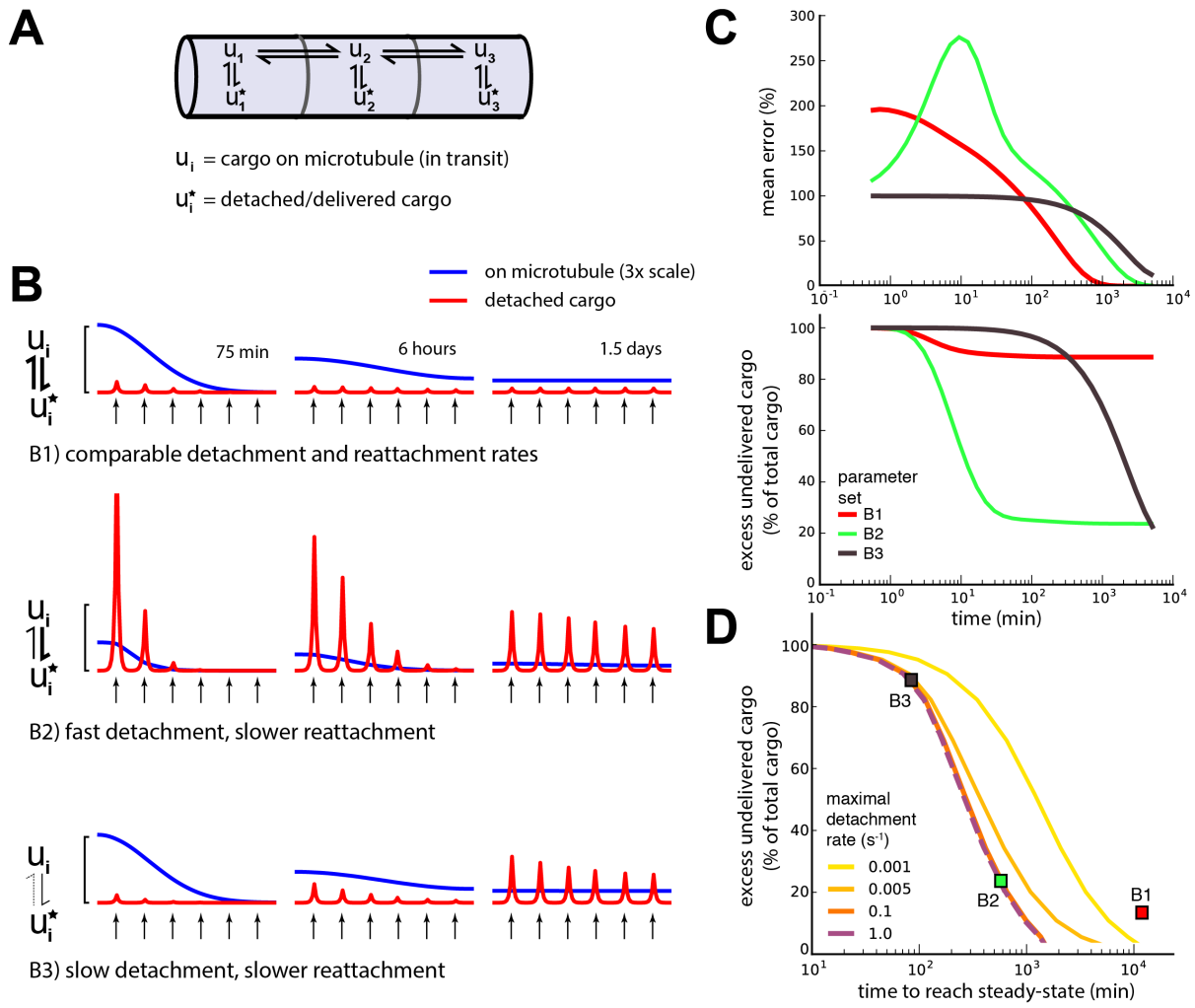

Figure 5 supplement 2. Adding a mechanism for cargo reattachment produces a further tradeoff between rate of delivery and excess cargo. **(A)** Schematic of mass-action model with reversible detachment of cargo. **(B)** Simulations of three illustrative parameter sets. As in figure 6, cargo is distributed to six demand hotspots (black arrows). Six evenly distributed demand hotspots are placed along a neurite with a biologically relevant length of 800 μm and an optimistic diffusion coefficient of 10 $\mu m^2/s$. The distributions of cargo on the microtubules (u_i, blue) and detached cargo ($u_i^\star$, red) are shown at three times points for each model. Top row, a model in which detachment and reattachment occur on similar timescales (fast convergence). Middle row, a model in which detachment happens on a faster timescale than reattachment (reattachment is still quite fast relative to trafficking rates; slow convergence). Bottom row, a model in which detachment occurs slowly, and reattachment occurs even slower (slow convergence). **(C)** Mean percent error in the distribution of detached cargo (top) and excess cargo (bottom) as a function of time for the three parameter sets shown in panel B. **(D)** Tradeoff curves between excess cargo and time to converge to steady-state. Fast reattachment rates caused large excess cargo (upper left corner); increasing reattachment decreased this excess, but also increased the convergence time (lower right corner). The tradeoff is present across four detachment timescales (yellow-to-purple lines) that span four orders of magnitude. Colored squares denote the position of the three parameter sets shown in panels B and C. A model was judged to read steady-state when the derivatives dropped below a set threshold, near zero (see *Methods*).